Proceedings of the 21st ICSMGE, Vienna, Austria, 14 – 19 June 2026. Pistrol, Adam & Schweiger (eds.)
Published by: ÖGG, Austrian Society for Geomechanics, Salzburg, Austria, ISBN 978-3-9503898-4-5
https://doi.org/10.53243/ICSMGE2026-2311

Significance of the earthquake motion records of the 2023 Türkiye-Syria earthquakes

Ikuo Towhata
Kanto Gakuin University, Yokohama, Japan, towhata.ikuo.ikuo@gmail.com

ABSTRACT: The 2023 earthquake sequence in Türkiye and Syria triggered devastating damage in buildings and infrastructures along the East Anatolian Fault. Among many seismic events during this sequence, the strongest one was the Pazarcık earthquake of *M*w = 7.8 at AM 4:17 local time on February 6th and the most damage occurred during this event. The author carried out a damage reconnaissance in early June, 2023, by visiting the sites of landslide, embankment failure, liquefaction and building damage. Among many notable findings, this paper addresses the characteristics of the seismic ground motion recorded during the Pazarcık earthquake, paying attention to the effect of the ground motion on building damage. The first issue is the substantially less extent of building damage in the hilly area of Kahramanmaraş as compared with the devastation in the alluvium plain of the same city. This difference is accounted for by the weaker acceleration in the hill due to the lack of well-known soil amplification of the ground motion. Of further interest is the greater extent of damage in the Southwestern part of the affected area such as Antakya and the 'southwest' direction is seemingly related with the direction of the fault rupture propagation. From this viewpoint, many acceleration records obtained and published by AFAD were interpreted to find that the acceleration intensity increased, the duration of motion decreased and the predominant period became longer towards southwest. To understand the cause of this spatial variation of the ground motion, a simple model was developed by which the fault rupture propagation velocity and the propagation of the emitted seismic wave were quantitatively considered. It was found, accordingly, that the high rupture propagation velocity (possibly supershear) and the superposition of many seismic impulses emitted from fault segments caused the abovementioned feature of the ground motion.

KEYWORDS: 2023 Turkey-Syria earthquake, fault rupture, ground motion, Fourier spectrum, supershear.

1 INTRODUCTION

The southeastern part of Türkiye (formal name of Turkey) was affected by a sequence of earthquakes in February, 2023, and many buildings were destroyed by the strongest Pazarcık earthquake of *M*w = 7.8. The author visited the affected regions in early June, 2023, for damage reconnaissance and got an opportunity to investigate the seismic conditions that triggered the severe damage. One of the peculiar issues encountered during the reconnaissance was that the damage extent was more serious towards the western end of the fault rupture and the author supposed that the western region underwent different nature of ground motion possibly affected by the regional geological and seismological conditions. This paper summarizes the author's study that was conducted on this issue.

2 BUILDING DAMAGE IN THE AFFECTED REGION

Figure 1 presents a map of southwest Türkiye where the East Anatolian Fault ruptured over 320 km. This event started in the central part, followed by rupture propagation first towards northeast and then turning-around towards the western end (Jia et al., 2023). This figure shows the location of the AFAD national seismological observation stations at which valuable acceleration records were obtained.

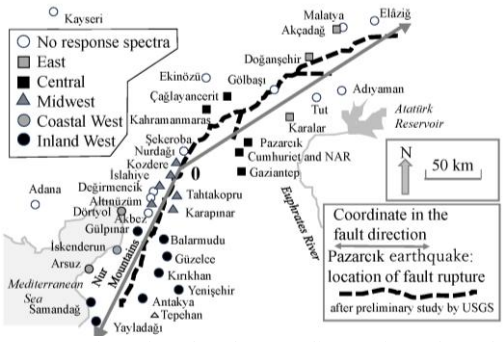

Figure 1. Location of earthquake recording stations along the East Anatolian Fault in SE Türkiye.

Figure 2. Substantial building damage in the area of alluvium in Kahramanmaraş near the middle part of the fault (see Figure 1).

Figure 3. Little damage in the hilly part of Kahramanmaraş.

Figure 4. Devastating damage in Antakya.

For many decades Türkiye has made efforts to elaborate seismic building design codes. Despite that, the building damage was very serious as shown in Figure 2. This was in a very clear contrast with little damage in the hilly part of the same city (Figure 3). Further, Figure 4 indicates the severer damage extent in Antakya of Hatay. The author surveyed the experts' opinions on this code-vs-reality discrepancy; Erdik (2001), Polat (2019), Onat et al. (2022), Ozturk et al. (2023) and Mertol et al. (2023). It was found that design and construction practices had such problems as inappropriate structural design, poor quality of materials, owners modification without considering the structural safety, insufficient public control of construction quality and legalization of illegal buildings. Although these social issues are important, they are not enough to account for the more devastating damage in Antakya as statistically indicated by the Middle East Technical University (2023) and Vuran et al. (2024).

3 EARTHQUAKE GROUND MOTION

The damage contrast between Figures 2 and 3 clearly verifies the local geological and topographical effects on seismic damage. In line with this, the acceleration records obtained in the hill and the alluvium of Kahramanmaraş (Figure 5) indicate different intensities; stronger in the alluvial plain. The percent evolution of shaking is defined by $\int \sqrt{EW^2 + NS^2}\,\mathrm{dt}$ (combination of the East-West and North-South components) and will be discussed in Figure 10. Figure 6 presents the acceleration time histories in Antakya which are evidently stronger than the records in Kahramanmaraş in consistent with more devastation.

Figure 7 shows the NS velocity time histories at the three sites presented in Figures 5 and 6. It is clearly shown that the peak value of the velocity (PGV) was the greatest in Antakya, while it was smallest in the hilly area of Kahramanmaraş where damage was not important at all (Figure 3). Noteworthy is the velocity pulses in Figures 7(b) and (c). There are discussions that such a velocity pulse (strong intensity with elongated period) plays a chief role in triggering seismic damage of structures (Morii et al., 2019; Chen et al., 2021).

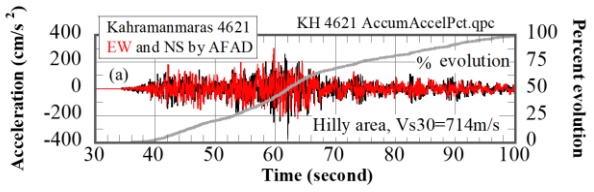

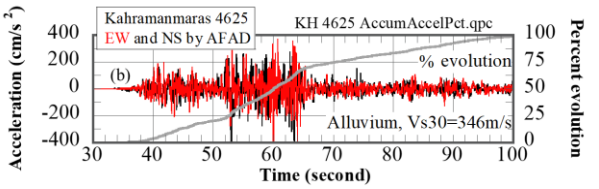

Figure 5. Acceleration time histories in the hill (a) and the alluvial plain (b) of Kahramanmaraş (recorded at AFAD Stations 4621 and 4625)

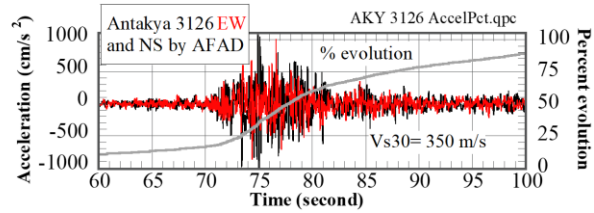

Figure 6. Acceleration time histories in the devastated part of Antakya (recorded at AFAD 3126 Station).

(a) NS velocity in hilly terrain of Kahramanmaraş (Station 4621)

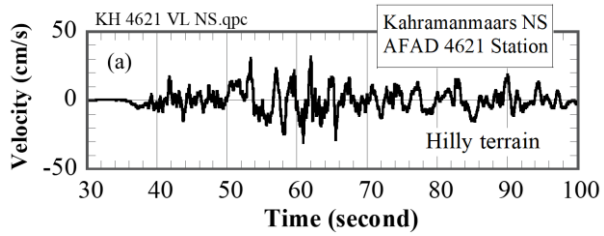

(b) NS velocity in alluvium of Kahramanmaraş (Station 4625)

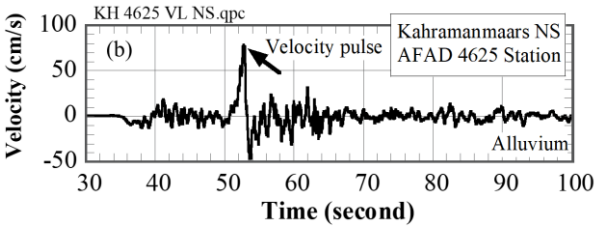

(c) NS velocity in Antakya (Station 3126)

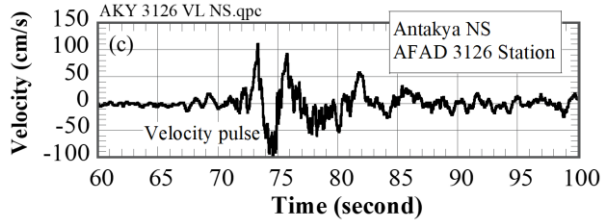

Figure 7. Velocity time histories recorded by AFAD.

4 SPATIAL VARIATION OF GROUND MOTION

This section addresses the variation of the seismic ground motion that were recorded at many places in the vicinity of the causative fault (Figure 1). Figures 8 and 9 plot the spatial variation of the peak acceleration (*PGA*) and velocity (*PGV*) near the causative fault as shown in Figure 1. The location of the observation sites is indicated by the fault parallel coordinate as shown in Figure 1 and is used hereinafter as the spatial index, having its origin at "O" in the figure and being taken positive westward while negative towards the east. Although both *PGA* and *PGV* exhibits significant ranges of variation most likely because of the local soil conditions and topography, there is a clear trend in the western half of the diagram (positive fault-parallel coordinate) that their upper bounds increase towards the west. Note that the rupture propagated towards the west as well in this section of the fault. Pitifully, no discussion is possible in the eastern region because of the malfunctioning of sensors.

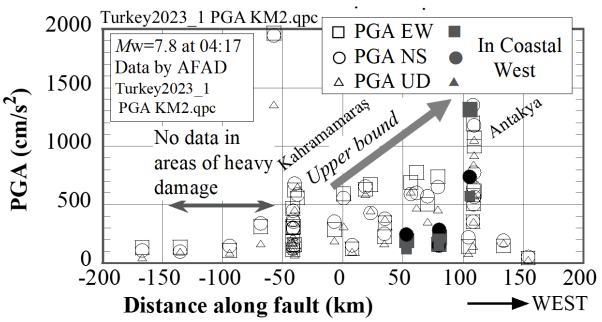

Figure 8. Variation of *PGA* (Peak Ground Acceleration) along the fault-parallel coordinate axis.

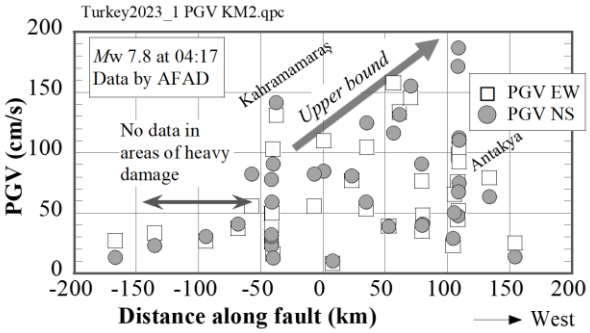

Figure 9. Variation of *PGV* (Peak Ground Velocity) along the fault parallel coordinate axis.

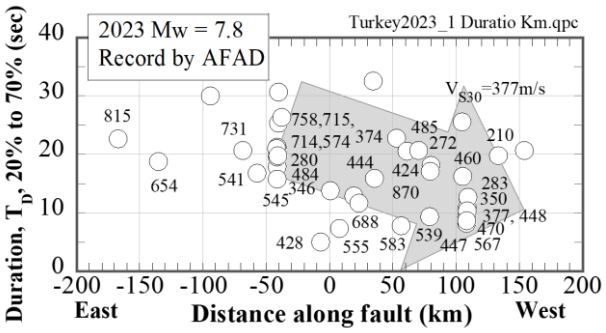

Figure 10. Spatial variation of duration of shaking along the fault-parallel coordinate axis.

Duration of strong ground motion is another factor that governs the damage extent of structures that are prone to the cyclic effects of shaking. In this paper, the duration, T_D, is defined by using the temporal evolution of $\int \sqrt{EW^2 + NS^2}\,dt$ of acceleration records that is plotted in Figures 5 and 6 in a percentile manner. In particular, the strong phase of shaking is defined in this study as time from 20% to 70% of the percentile evolution. The duration thus defined is plotted in Figure 10 against the fault-parallel coordinate. Note that the substantial range of variation is not likely due to local soil conditions because the V_{S30} values (the mean *S*-wave velocity in the top 30-m soil) do not exhibit a correlation with the duration. Interestingly, there is a background trend in the western area that the duration becomes shorter towards the west. This point can be confirmed by comparing Figures 5 and 6 as well. The shorter duration in the western area may contradict with the building damage extent that was severer towards the west (Figure 4). Presumably, the damaged buildings were brittle and destroyed by a few strong impulses. Discussion will be made of the impulse later on.

The frequency component and the predominant frequency of the ground motion are important features that govern the influence on structures. In this regard, the Fourier expansion series (similar to the Fourier Spectra) were calculated for several records and exhibited in Figure 11. The concerned AFAD stations are designated by 4-digit numbers herein. In Kahramanmaraş, first, the hilltop records at two sites (a) have lower spectral values than those in the alluvial plain (b). Thus, the less extent of damage in the hilly terrain (Figure 3) is understandable. Especially, the weak components in the low frequency range (<2 Hz in this paper) produce weak velocity after time integration (Figure 7(a)), which is consistent with the lack of damage; refer to an empirical correlation between velocity and damage extent (e.g., Kostinakis et al., 2015). In contrast, the spectra in Antakya (Figure 11(c)) have stronger spectral values over the entire frequency range than the Kahramanmaraş records and this is particularly the case in the low frequency range of the records at the AFAD 3123 and 3124 Stations. Importantly, the low-frequency spectra of the Antakya spectra are remarkably stronger than the high-frequency spectra, implying strong velocity in Antakya.

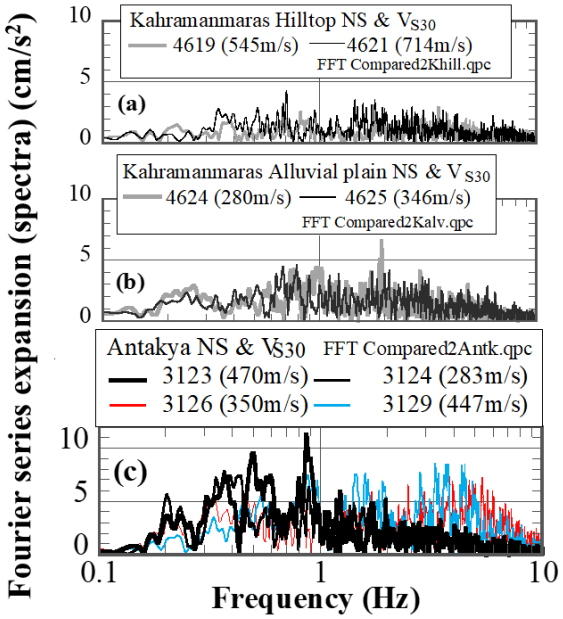

Figure 11. Fourier series expansion of NS acceleration.

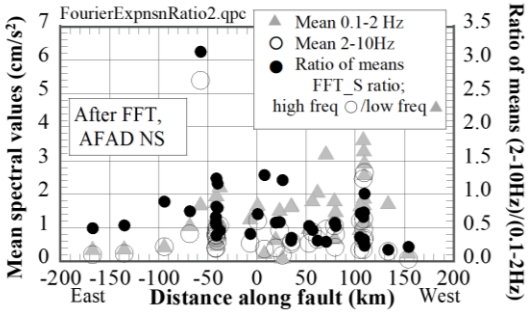

Figure 12. Variation of low and high frequency spectra along the fault parallel coordinate axis.

The contrast of the spectral levels between low (0.1 - 2 Hz) and high (2 - 10 Hz) frequency ranges are examined in Figure 12. It is seen here that the mean spectral values in both high and low frequency ranges (▲ and ○) increase towards the western end of the rupture, which is consistent with the variation of *PGA* (Figure 8). Noteworthy is the variation of their ratio (●) that is defined by "*High frequency / Low frequency*" and decreases westwards. This implies that the low frequency components become more predominant in the western part of the fault rupture as was typically illustrated in Figure 11(c). Finally, Figure 13 compares the velocity response spectra in Kahramanmaraş and Antakya. As expected, the Antakya spectra at four sites are greater than those in Kahramanmaraş and the hilly area of Kahramanmaraş exhibits the weakest response spectra. This is consistent with the observed damage extent.

In summary, the acceleration records are characterized by greater peak values (Figures 8 and 9) with shorter duration (Figure 10) and lower predominant frequency (Figures 11 and 12) towards the western end of the fault. These characteristics are independent of local conditions. For more details, refer to Towhata et al. (2025).

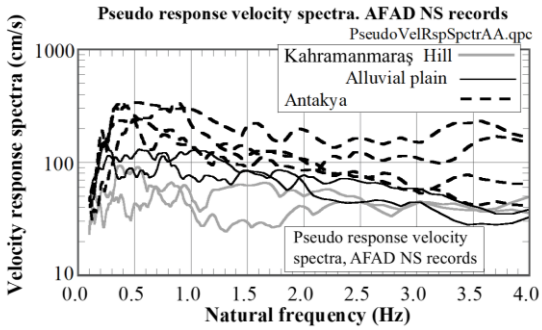

Figure 13. Comparison of velocity response spectra (5% critical damping ratio) in Kahramanmaraş and Antakya.

5 HIGH RUPTURE PROPAGATION VELOCITY

The author attempts here to explain the mechanisms that produced the three characteristics of ground motion as stated above by paying attention to the rupture propagation velocity, V_R, of the causative fault. Figure 14 exhibits the relationship between the arrival time of the *S*-phase of the ground motion and the fault-parallel coordinate. It is found here that the first arrival occurred in the central part, followed by the eastern part and then the western part. This sequence verifies the rupture propagation, first towards the east and to the west, as mentioned above. It is possible to approximately assess V_R by using the gradient of the data, which is between 3 and 5 km/s. Thus, it is very likely near the western part of the fault (near Antakya in particular) that V_R exceeded the *S*-wave velocity (Vs about 3 km/s) of the base rock. Then, what happens if $V_R > V$s?

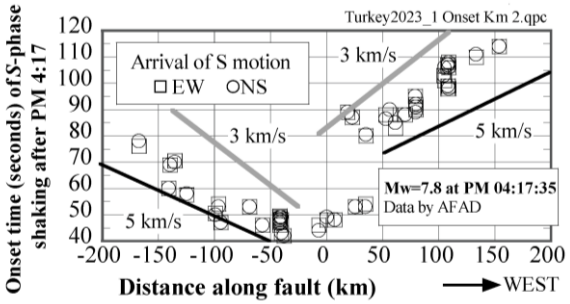

Figure 14. *S*-wave arrival time during the earthquake.

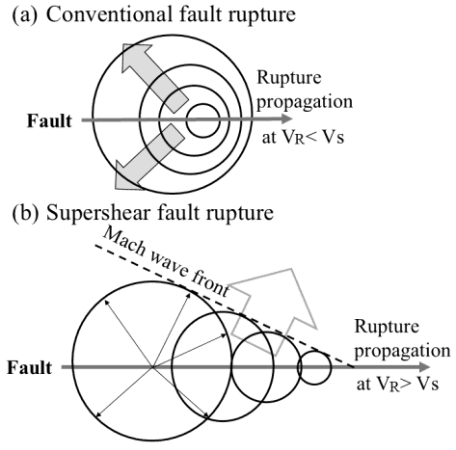

Figure 15. Wave front of supershear.

Figure 15 illustrates the seismic wave propagation from a sequence of fault rupture for which the source of energy emission propagates at a rate of V_R and the emitted energy propagates at Vs. In case of $V_R < V$s, the conventional wave propagation occurs and the wave fronts form nesting circles (Figure 15(a)). Conversely when $V_R > V$s, which is called supershear, a wave front is formed as a tangent line to the wave front circles and energy is condensed within the linear Mach wave front (Figure 15(b)). Supershear is not a common phenomenon but there are a few examples; the 1979 Imperial valley earthquake of Mw = 6.5 in California (Archuleta, 1984), the 1999 Izmit earthquake of Mw = 7.6 (Bao et al., 2022), the 2018 Palu/Sulawesi earthquake of Mw = 7.5 in Indonesia (Socquet et al., 2019) and more.

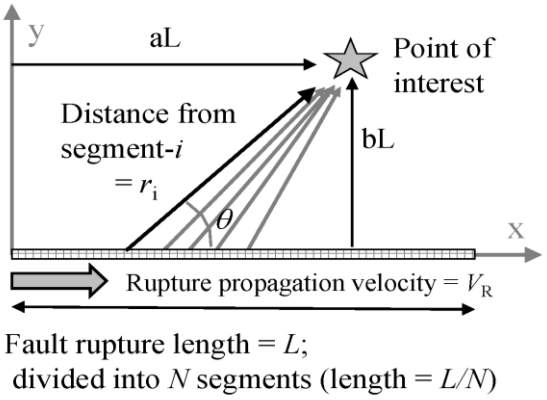

Figure 16. Model to reproduce supershear effect on ground motion.

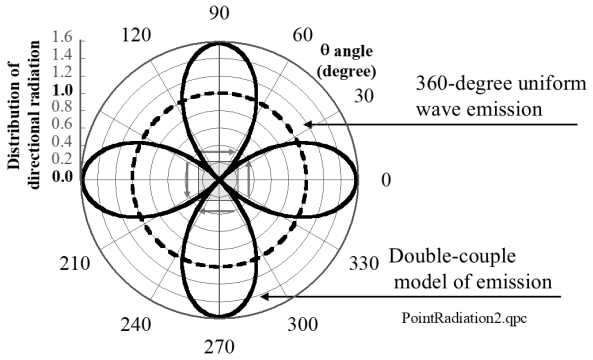

Figure 17. Double-couple model of wave transmission from a small segment rupture.

The consequence of supershear fault rupture was numerically reproduced by using the model in Figure 15. First, the distance between the *i*-th segment of fault rupture and the point of interest in Figure 16 (X=*al*, Y=*bL*) is given by

$$r_i = \sqrt{\left\{X - \left(i - \frac{1}{2}\right)\frac{L}{N}\right\}^2 + Y^2} \qquad (1)$$

Accordingly, the time of wave arrival at the point of interest is given by

$$t_i = \frac{\sqrt{\left\{X - \left(i-\frac{1}{2}\right)\frac{L}{N}\right\}^2 + Y^2}}{V_S} + \frac{\left(i-\frac{1}{2}\right)\frac{L}{N}}{V_R} \qquad (2)$$

in which time is set equal to zero at the initiation of fault rupture at its left end (Figure 16), and 'i' designates the fault segment from which the particular wave starts; $i = 1 \sim N$. Then, the arrival time is normalized as

$$T_i \equiv \frac{V_S}{L} t_i = \sqrt{\left(a - \frac{i-\frac{1}{2}}{N}\right)^2 + b^2} + \frac{V_S}{V_R} \times \frac{i-\frac{1}{2}}{N} \qquad (3)$$

Note that $t=L/V_R$ and $T=V_S/V_R$ when the fault rupture reaches the end of the fault.

By denoting the wave energy emission from a unit length of fault rupture by 'e', the energy emission from the entire fault is given by Le and the energy from one segment by Le/N. Accordingly, the energy that arrives at the point of interest is given by

$$e_i = \frac{1}{2\pi r_i}\left(\frac{Le}{N}\right)F(\theta) \tag{4}$$

per unit area in which $F(\theta)$ designates for the directional effect of energy emission (Figure 17) and is defined as

$$\left.\begin{array}{ll} F(\theta) \equiv \left(\frac{2}{\pi}\right)|cos2\theta| & \text{for a double} - \text{couple mechanism} \\ F(\theta) = 1 & \text{for a hypothetical uniform radiation} \end{array}\right\} \tag{5}$$

Note further that the factor of $2/\pi$ herein makes the total energy discharge over 360-degree direction equal to the total energy of uniform radiation (compare two curves in Figure 17). Then, the energy arrival per unit area is normalized as

$$E_i \equiv \frac{e_i}{e} = \frac{F(\theta)}{2\pi N\sqrt{\left\{a-\frac{\left(i-\frac{1}{2}\right)}{N}\right\}^2+b^2}} \tag{6}$$

For simplicity, the energy emission is assumed homogeneous over 360 degrees in this paper ($F(\theta)=1$) but, in reality, it follows a double couple mechanism of rupture (Aki, 1960) and varies with the direction. The cumulative normalized energy and the rate of energy arrival or energy arrival per unit area and unit time (equivalent with the intensity of shaking) are calculated respectively by

$$\sum E_i \text{ and } \frac{d}{dT_i}\sum E_i \tag{7}$$

Figure 18 illustrates the time history of energy arrival per unit area and per unit time in case of non-supershear fault rupture ($V_R = 0.75V_S$). For this diagram, the arrivals of energy impulses from a segmental fault rupture were calculated first and then the energy arrival per time was calculated and plotted. This energy arrival per time is related with (*the shaking velocity*)^2. See also in this figure that the duration of shaking is about 0.5 normalized time. In contrast, Figure 19 illustrates the energy arrival per time for a supershear fault rupture ($V_R = 1.2V_S$). The intensity of the arrived energy starts with the maximal and then decreases. This feature is different from the non-supershear energy arrival in Figure 18 where the energy increases first and then decreases. The initiation with the maximal in Figure 19 stands for the arrival of the wavefront (Figure 15(b)) in which the wave energy is condensed within a short time. Importantly, the energy arrival per time is profoundly greater in the supershear case (Figure 19) than in the non-supershear case (Figure 18), indicating that the supershear ground shaking is stronger than that of non-supershear earthquakes, if other issues are identical. Further, the duration is shorter than 0.1 normalized time and is shorter in the supershear case (Figure 19) than the duration of the non-supershear earthquake motion (Figure 18). These features are consistent with the findings from the real earthquake as stated above.

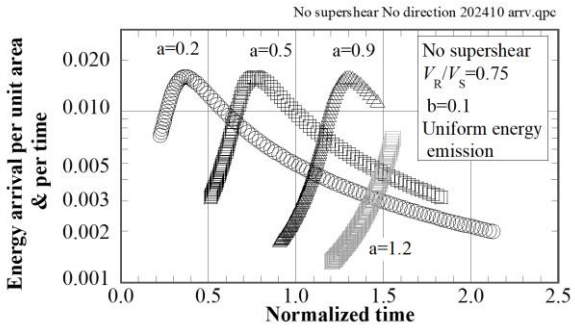

Figure 18. Energy arrival per time in case of non-supershear fault rupture.

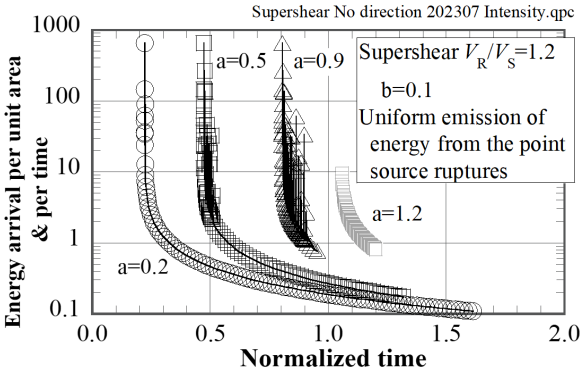

Figure 19. Consequence of supershear fault rupture.

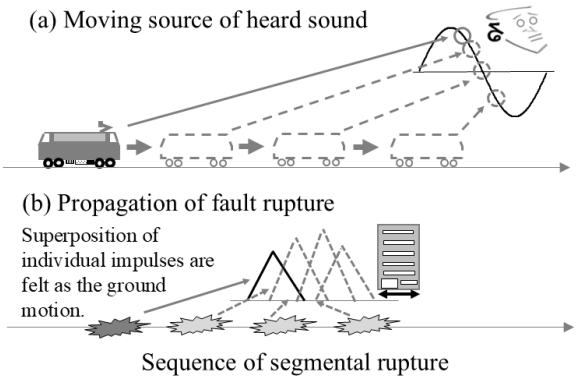

Figure 20. Schematic diagrams on difference between the Doppler effects of sound with the source coming towards a listener and the seismic impulses coming towards a damage site.

The remaining question to be answered concerns the reason of the elongated period or reduced shaking frequency (Figures 12 and 13). It should be recalled that the Doppler effect of sound propagation is opposite from this; sound frequency is made higher when the source is coming to the listener (Figure 20(a)). At this moment, the answer is the superposition of many impulses with a short time lag; the impulses coming from the segmental rupture sequence along a fault.

To validate this idea, a conceptual superposition was calculated by using a series of simple impulse, starting sequentially from the ruptured segments in a fault, as shown by the gray curve in Figure 21. Those impulses arrive at the points of interest at different times and intensities, depending on the propagation distance (Figure 22(a)). The time lag among the arrivals varies with the rupture propagation velocity, V_R.

The results are demonstrated schematically (without unit) in Figures 22(b) and (c) where the individual impulses are drawn in gray, while the superposition in black color. When the time lag is short (30 degrees in terms of phase angle), the

superposition produces one long period of motion (Figure 22(b)). When V_R is slower, the lag becomes longer (60 degrees) and the superimposed long-period component is not evident anymore (Figure 22(c)). Thus, rapid propagation of fault rupture can make impulse superposition more significant and the elongated period of shaking. It may be possible that this significant superposition is the cause of the velocity pulse in Figure 7 but further discussion is needed on this issue.

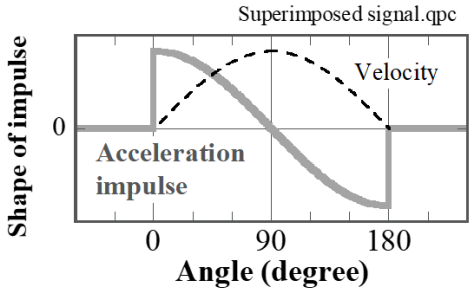

Figure 21. Idealization of acceleration impulse by a half cycle of cosine function (gray curve) that is equivalent with a half-cycle cosine function of velocity impulse (black broken curve).

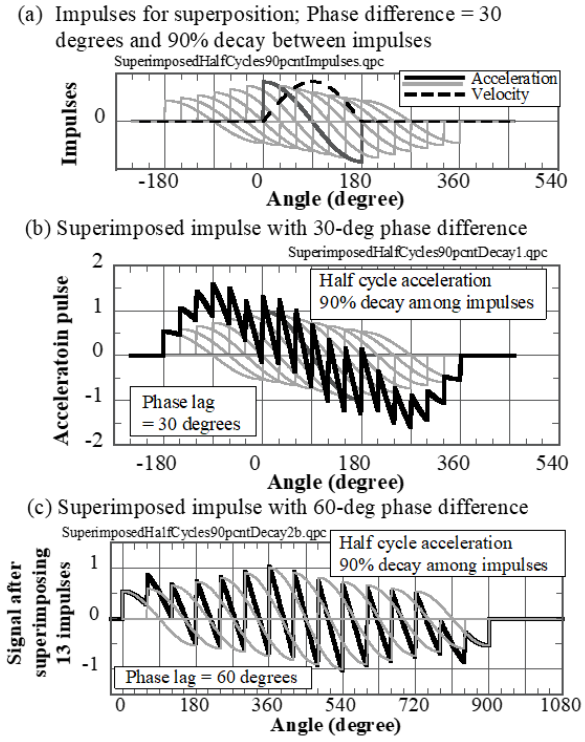

Figure 22. Elongation of ground motion period by superposition of individual impulses coming from segmental fault rupture; individual impulses shown by gray curves and their superposition by black curve, respectively, in (b) and (c).

6 CONCLUSIONS

The earthquake ground motion during the event in 2023, Türkiye, was studied. The extent of structural damage appeared more substantial towards the western part of the affected area along the causative fault. To understand this spatial variation, the observed acceleration records were interpreted to find that the acceleration/velocity intensities tended to increase, the duration of shaking became shorter and the predominant period of motion got shorter towards the west. This directional effect was in line with the direction of the fault rupture propagation in the concerned area. To further understand the reason of this spatial difference, a simple fault-rupture model was developed and it was concluded that the mechanism of supershear fault rupture is likely the cause of the peculiar nature of the spatial effect of the ground motion along the fault-parallel coordinate.

7 ACKNOWLEDGMENT

The author expresses his sincere thanks to those who carried out the field work together, who are namely Prof. Pınar Özdemir Çağlayan, Dr. Gökçe Tönük, Mr. Uğur Can Erginağ and Dr. Seda Sendir Torisu. AFAD of the government of Türkiye is appreciated for its publication of the recorded earthquake motion records.

8 REFERENCES

Aki, K., 1960. Study of earthquake mechanism by a method of phase equalization applied to Rayleigh and Love waves. *Journal of Geophysical Research,* 65(2), 729-740.

Archuleta, R.J., 1984. A faulting model for the 1979 Imperial Valley earthquake of M_L=6.6. *Journal of Geophysical Research: Solid Earth,* 89(B6), 4559–4585.

Bao, H., Ampuero, J.P., et al., 2019. Early and persistent supershear rupture of the 2018 magnitude 7.5 Palu earthquake. *Nature Geoscience.* 12(3), 200–205.

Chen, G., Xia, M. et al., 2021 A possible mechanism of earthquake-induced landslides focusing on pulse-like ground motions. *Landslides,* 18(5), 1641-1657.

Erdik, M., 2001. Report on 1999 Kocaeli and Düzce (Turkey) earthquakes, *Structural Control for Civil and Infrastructure Engineering*, publ. World Scientific, 149-186.

Jia, Z., Jin, Z. et al., 2023. The complex dynamics of the 2023 Kahramanmaraş, Turkey, Mw 7.8-7.7 earthquake doublet, *Science,* 381(6661), 985-990.

Kostinakis, K., Athanatopoulou, A. et al., 2015. Correlation between ground motion intensity measures and seismic damage of 3D R/C buildings. *Engineering Structures,* 82, 151-167.

Mertol, H.C., Tunç, G., et al., 2023. Investigation of RC Buildings after 6 February 2023, Kahramanmaraş, Türkiye Earthquakes, *Buildings,* 13(7), p. 1789.

Middle East Technical University, 2023. Preliminary Reconnaissance Report on February 6, 2023, Pazarcık Mw=7.7 and Elbistan Mw=7.6, Kahramanmaraş-Türkiye Earthquakes, Report number *METU/EERC* 2023-01.

Morii, T., Sugino, M. and Hayashi, Y., 2019. Response and damage of buildings due to the pulse-like ground motions near fault. *Journal of JAEE,* 19(6), 139-151(in Japanese).

Onat, O., Yön, B. et al., 2022. Field reconnaissance and structural assessment of the October 30, 2020, Samos, Aegean Sea earthquake: an example of severe damage due to the basin effect, *Natural Hazards,* 112, 75–117.

Ozturk, M., Arslan, M.H., and Korkmaz, H.H., 2023. Effect on RC buildings of 6 February 2023 Turkey earthquake doublets and new doctrines for seismic design, *Engineering Failure Analysis,* 153, p.107521.

Polat, Z.A., 2019. Analysis of the regulation of "Zoning Reconciliation" in local governments, *Planlama,* 29(3), 202–209.

Socquet, A., Hollingsworth, J., et al., 2019. Evidence of supershear during the 2018 magnitude 7.5 Palu earthquake from space geodesy. *Nature Geoscience,* 12(3), 192-199.

Towhata, I., Çağlayanb, P.Ö., et al., 2025. Reconnaissance and discussion on ground motion induced by the 2023 Türkiye-Syria earthquake. *Journal of Earthquake Engineering,* 29(5), 981-1022.

Vuran, E., Serhatoğlu, C. et al,. 2025. Damage observations of RC buildings from 2023 Kahramanmaraş earthquake sequence and discussion on the seismic code regulations. *Bulletin of Earthquake Engineering,* 23, 1153–1182.